



Quantitative In-situ Analysis of Water Transport in Concrete Completed Using X-ray Computed Tomography

Tyler Oesch¹ · Frank Weise¹ · Dietmar Meinel¹ · Christian Gollwitzer¹

Received: 12 April 2018 / Accepted: 8 November 2018 / Published online: 16 November 2018
© The Author(s) 2018, corrected publication 2019

Abstract

This paper describes a novel methodology for quantitative in-situ moisture measurement without tracking agents using X-ray computed tomography (XCT). The high levels of greyscale precision required for the measurement of moisture without tracking agents resulted in the need for an additional image calibration procedure to correct for water-related X-ray scattering and for equipment-variability-related artefacts arising during in-situ testing. This calibration procedure was developed on the basis of existing principles of XCT image correction. Resulting images of moisture distribution exhibit a high level of agreement with expected material behaviour. This research demonstrated that XCT can be successfully used to measure both moisture front movement over time and changes in 3D moisture distribution within samples. This approach to moisture measurement lays the groundwork for the planned future investigation of the interaction between cracking induced by varying chemical and mechanical processes and water transport in concrete.

Keywords X-ray computed tomography (XCT) · In-situ testing · Water transport · Quantitative moisture measurement · Concrete

1 Problems and Objectives

The durability of concrete is significantly affected by its hygral properties. This is due to the fact that many of the most important damage processes in concrete only occur in the presence of water. This is true for alkali-silica reaction (ASR) and sulphate attack as well as for expansive freezing and freeze–thaw attack. However, the moisture also plays a central role in the case of explosive spalling in high-density, high-performance concretes during fire or other high-temperature exposure. Given its important role in concrete behaviour, the accurate measurement of moisture distribution in concrete is of central importance.

✉ Tyler Oesch
tyler.oesch@bam.de

¹ Bundesanstalt für Materialforschung und –prüfung (Federal Institute for Materials Research and Testing), Unter den Eichen 87, 12205 Berlin, Germany

2 State of the Art

Until recently, the direct measurement of moisture was carried out using primarily the gravimetric (also known as the Darr weighing) method as well as the calcium carbide method (also known as the CM method) (ASTM 2010, 2018). Given the destructive nature of both of these testing techniques, various alternative indirect moisture measurement techniques have also been developed. These techniques can be separated by the moisture-affected physical properties of building materials that they measure. These include the measurement of electrical, thermal, hygrometric, and radiometric properties, respectively. A thorough description and evaluation of these various moisture measurement techniques can be found in Weise (2008).

Previous research has demonstrated that for accurate simulation of liquid transport in complex material structures, both measurements of internal material composition (such as pore and crack characteristics) and time-resolved measurements of changing moisture conditions are necessary (Bultreys et al. 2016; Van Belleghem et al. 2016; Van Stappen et al. 2014). For the concrete material that was the focus of this research project, the interacting fluid-transport and crack-formation processes made a quantitative analysis of the temporal changes in the moisture distribution essential for the development of planned future simulations. Precise measurements of moisture were also needed for further clarification of damage induced through various mechanisms at the meso- and microscale. For such an application, the range of appropriate moisture measurement techniques becomes limited to only the radiological methods. These techniques include methods based on nuclear magnetic resonance (NMR), neutron scattering-based methods (Visvalingam and Tandy 1972), neutron computed tomography (NCT), and X-ray computed tomography (XCT).

NMR is used extensively for moisture measurement within concrete materials (RILEM 2005). However, NMR equipment capable of measuring 3D images of moisture distribution in concrete samples is not yet widely available in most materials research laboratories. Given that NMR measurement techniques also fail to provide high-resolution images of the internal material structure, such as cracking and aggregate distribution, they were not particularly suitable for this specific research project.

NCT is an alternative method for measuring water in concrete and other materials. One advantage of NCT is that hydrogen-rich compounds, such as water, show a higher contrast in the resulting images than in XCT images (Cnudde et al. 2007, 2008; Derluyn et al. 2013; Dewanckele et al. 2014; Dierick et al. 2005; Masschaele et al. 2004; Weber et al. 2013). Although the lower sharpness of NCT images (in comparison with XCT ones) has traditionally been a limitation of this method, recent work has also demonstrated that neutron radiography images with improved sharpness can be obtained using iterative de-blurring techniques (Masschaele et al. 2005). Using high-flux neutron sources, it is even possible to obtain images of very high speed material behaviour processes (Hillenbach et al. 2005).

However, given that one focus of this research effort was to develop quantitative moisture measurement techniques that could be implemented using common laboratory equipment, the XCT measurement method was selected rather than NCT. While NCT relies on the use of large beamline scanning facilities, which are limited in number and have corresponding access-time constraints, XCT methods use widely available X-ray scanning systems, which now form a part of most large materials research laboratories.

A number of studies have shown the potential of X-ray radiology to detect pure water within concrete samples, including quantification of changes in moisture content (Bentz and Hansen 2000; Cnudde et al. 2015; Kaufmann et al. 2015; Lukovic and Ye 2015; Pease et al. 2012; Roels and Carmeliet 2006). A number of studies have also extended moisture

measurement to XCT. Many of these studies have focused on the filling of void space in porous or granular materials by water (Peng et al. 2015; Wildenschild et al. 2002, 2005). Although this approach may be sufficient for certain geological materials, it is not applicable to concrete, where the cement matrix can absorb significant quantities of water. The direct measurement of moisture content within the mortar matrix of concrete is particularly difficult because of the high initial density of the material, low density changes caused by moisture transport, variability in performance of the X-ray scanning equipment over time, and the varying X-ray scattering artefacts caused by changing water conditions in a highly heterogeneous material structure.

To overcome these challenges, some studies have included the introduction of contrast agents, such as CsCl, into the water in order to improve contrast (Boone et al. 2014; Yang et al. 2015). For the material described in this paper, however, the use of such agents was undesirable because the tracking agents could have an impact on not only the water viscosity and capillary bond, but on the chemical reactions that occur between water and unhydrated cement within the concrete matrix. Recent research has demonstrated that small moisture changes can also be detected through the use of phase-contrast imaging (Yang et al. 2016a, b; Yang et al. 2018). Although this method has great potential for future research applications, at the present time the grating systems necessary for its implementation are still uncommon within typical laboratory XCT systems.

Given these limitations, most of the in-situ XCT investigations of small moisture changes that have not used either contrast agents or phase-contrast imaging have relied either on qualitative assessments of visible moisture-related changes, on quantitative assessments of changes in sample attenuation without ever directly converting these attenuation measurements into moisture percentage estimates, or on quantitative assessments of parameters, such as water-front movement, that are not directly reliant on accurate moisture percentage measurements (Stelzner et al. 2017; Weise et al. 2007; Weise et al. 2006). For this reason, the current project was developed with the goal of extending the capabilities of the widely available XCT measurement method to include quantitative analysis of small moisture percentage changes within the concrete matrix during capillary water transport.

3 Material and Method

3.1 Sample Fabrication

Two cylindrical concrete samples with diameters of 50 mm and heights of 270 mm served as the basis for these experiments. These samples were cored from a concrete beam with dimensions of $27 \times 50 \times 200$ cm³. Because of the ASR-related focus of this research, it should also be mentioned that alkali-sensitive aggregates were used for the coarse-aggregate component of the concrete mix recipe. Detailed characteristics of this concrete mix in its fresh and cured states are provided in Tables 1 and 2.

3.2 Computed Tomography Scanning Procedure

Following sample extraction, XCT was used for evaluating moisture behaviour in both of the drilling cores during the water transport experiments, which were conducted based on the DAFstb standard (1991). The goal of these experiments was to determine changes in both the average moisture profile over the height of the samples and the 3D distribution of

Table 1 Concrete composition

Type and fraction of aggregate	(vol%)	
Sand from the Rhine river valley with size 0–2 mm		28
Quarried aggregate from the Upper Rhine river valley with size 2–8 mm		15
Quarried granodiorite aggregate with size 8–16 mm		27
Quarried granodiorite aggregate with size 16–22 mm		30
Cement		
CEM I 42.5 N (sd) (FGSV 2007); [Na ₂ O _{equ.} : 0.73 wt%]	(kg/m ³)	360
Additive		
LPS A 94	(wt% of cement content)	0.2
Water/cement ratio		0.42

Table 2 Selected parameters of fresh and hardened concrete

Fresh properties		
Air content	(vol%)	5.0
Density	(kg/m ³)	2330
Degree of compaction	(–)	1.24
Hardened properties		
Tensile strength $f_{ct,fl}$ (measured during four-point bending on the 56th day after sealed storage)	(MPa)	5.1 (0.19) ^a

^aMean value (standard deviation)

moisture throughout the cores. This experimental data could then be used as the basis for more advanced simulations of water transport and ASR damage mechanisms in concrete.

During the water transport testing, the core samples were placed within an in-situ water exposure apparatus developed specially for this purpose and scanned within a laboratory XCT machine. The water exposure apparatus contained a small pump, which ensured that the bottom surface of the sample was constantly in contact with water throughout the testing period (Fig. 1). The cylindrical surface of the sample was coated with a polymer layer to ensure a one-dimensional moisture transport in the concrete specimen. This layer prevented water seepage and evaporation from the sides of the sample during testing.

The XCT measurements were taken using a custom-built micro-XCT system equipped with a 225 kV X-ray source manufactured by X-ray WorX GmbH and a 2048x2048 pixel detector manufactured by Perkin Elmer, Inc. The X-ray source settings during all of the scans were 180 kV acceleration voltage and 160 μ A tube current. The X-ray beam was passed through a 1-mm-thick copper plate that was positioned between the X-ray source and the sample in order to filter out unwanted low-energy X-rays, reduce the beam hardening effect, and improve image quality. XCT scans were conducted at increments of 1 h, 3 h, 6 h, 1 day, 2 days and 3 days. During each scan, 2D projection images were collected at 600 equally spaced rotation increments. For each projection image, a total of three individual, one-second exposure images were collected and averaged. This resulted in a total time of approximately 30 min for each scan.

During each scan, binning, which is essentially a form of pixel averaging, was used to improve the signal-to-noise ratio. During this binning process, the size of the 2D projection

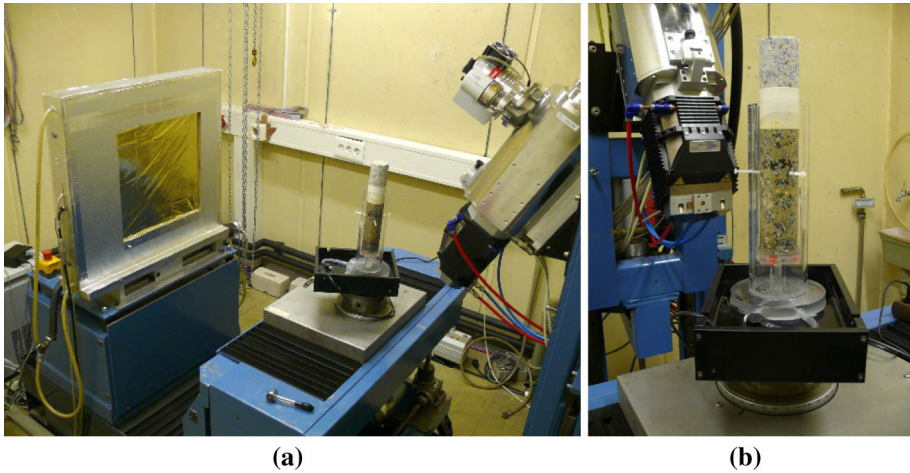


Fig. 1 Overall view of measurement arrangement (a) and detail view of the in-situ water exposure apparatus (b)

Table 3 Experimental measurement program for each specimen

XCT scan number	Water exposure duration (h)	Actual starting time for each XCT scan calculated in terms of the total time since the start of the experiment (h)
1	1	1
2	3	3.5
3	6	7
4	24	25.5
5	48	50
6	72	74.5

images was reduced by a factor of four and the size of the resulting 3D reconstructed images was reduced by a factor of 64. Since each voxel, which is the name for a 3D pixel, in the resulting reconstructed images represented a binned average of the 64 voxels that would have been presented in an image without binning, this resulted in images with high signal-to-noise ratio that were also of reasonable size for image processing.

During initial testing with the water exposure apparatus, it became clear that X-ray scattering effects due to water had a major impact on the pixel-greyscale distribution within the images. This effect was most severe at the base of the sample, where the apparatus ensured the presence of a constant pool of water. To reduce this effect, the water exposure apparatus was temporarily drained during XCT scanning for later experiments. Because the water exposure was eliminated during scanning, the XCT scanning times were not included in the calculation of the water exposure duration (Table 3). A flow diagram of the scanning process is depicted in Fig. 2.

A simple subtraction of the scanning period from the overall water exposure time does not, however, fully account for the impact of the interruption in water exposure on capillary flow, especially during the initial phases of re-exposure to water following the scan. The magnitude

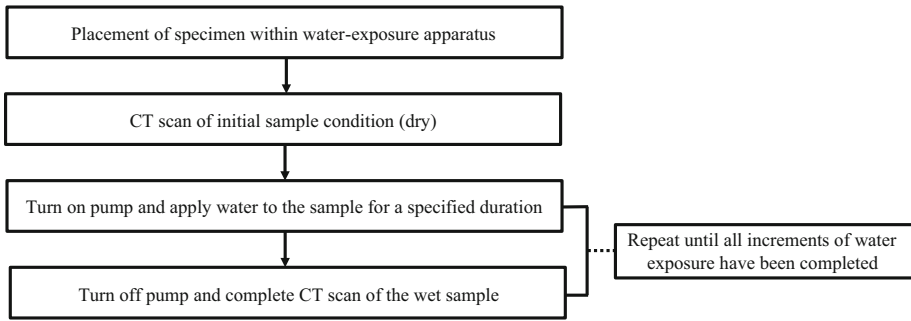


Fig. 2 Flow diagram of the scanning process

of the differences between moisture distributions during ideal continuous flow and during the interrupted flow of these experiments is very difficult to estimate. These differences are, however, considered to be most significant during initial stages of testing when the moisture conditions are changing most rapidly and to become relatively insignificant during later stages, when the water front has both slowed considerably and moved far from the water exposure surface.

Given that moisture conditions in the samples continued to evolve during the 30 min scanning period, the moisture measured in each resulting image represents an average of moisture conditions over the scanning period. Blurring in the resulting images due to this 30 min acquisition process was expected to be most severe both during the initial scans, when the moisture front was moving the fastest, as well as close to the edge of the moisture front in all scans, where moisture conditions were changing most rapidly. Overall, however, despite this blurring effect, moisture changes within this particular concrete material appeared to progress slowly enough that it was still possible to obtain high-quality images of moisture conditions in the samples, even during initial stages of testing.

3.3 Moisture Measurement using Conventional Image Processing Approaches

Following the experiments, 3D attenuation images were reconstructed using an in-house software developed by the Bundesanstalt für Materialforschung und –prüfung (BAM) in Berlin, which uses the Feldkamp algorithm (Feldkamp et al. 1984). All subsequent image analysis was completed using the program MATLAB (Mathworks 2018). In order to assess changes in moisture distribution, later XCT images were directly subtracted from the initial (dry-state) image (Eq. 1). 16-bit greyscale images were used throughout this analysis for better greyscale resolution, since 8-bit greyscale depth turned out to be insufficient to represent the small density changes due to the moisture transport.

$$D_{ijk} = I_{2ijk} - I_{1ijk} \quad (1)$$

D_{ijk} difference image, I_{1ijk} initial image of dry sample, I_{2ijk} subsequent image of wet sample.

By imposing a consistent greyscale threshold onto these difference images, it was possible to depict the progression of water into the sample as a function of time (Fig. 3).

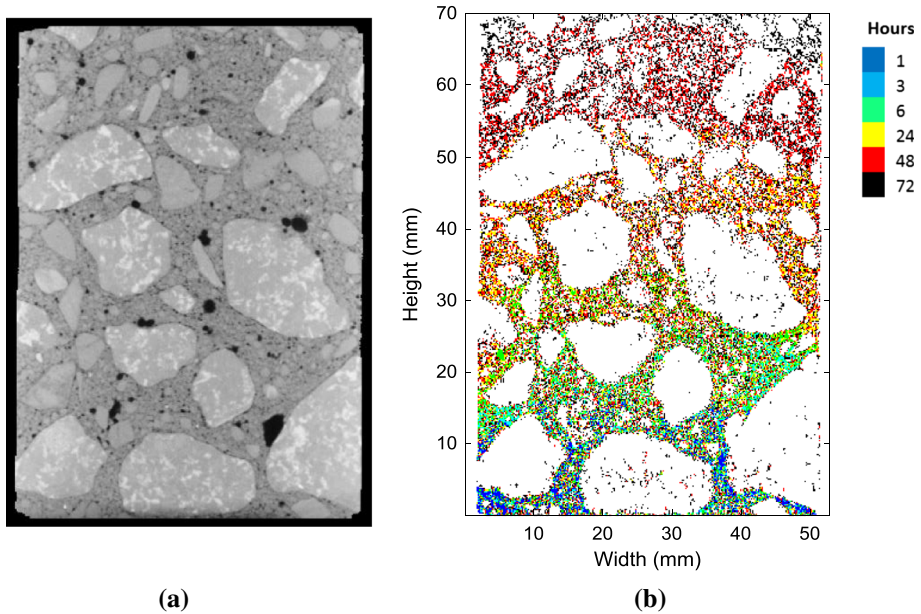


Fig. 3 XCT image of sample 1 (a) and depiction of time-based water transport measured using XCT (b)

3.4 Newly Developed Image Processing Techniques for Moisture Quantification

3.4.1 Identification and Investigation of Image Artefacts

In order to successfully measure 3D moisture percentage change, greyscale depth within the subtraction images had to be directly correlated with moisture percentage and quantified. Such a correlation was constructed by identifying the greyscale depth at the centre of a water-filled pore within one of the subtraction images. This greyscale depth was taken to represent a 100% change in moisture percentage (i.e. a transition from air to pure water). All other greyscale depths were then linearly scaled from this fully saturated calibration point to a greyscale depth of zero, which was considered to represent no change in moisture characteristics.

Optimally, greyscale depths within the centre of larger and more numerous water-filled pores would have been analysed to select the 100% moisture change calibration point value, but, unfortunately, only one water-filled pore was visible within these images and it was of only intermediate size. For future testing programs, the use of reference samples with embedded, water-fillable hoses or containers could be useful for more precisely defining the 100% moisture change greyscale calibration point.

These moisture percentage calculations required a much higher level of greyscale precision than is typical for most XCT research and the images proved to be highly sensitive both to the variation in performance of laboratory XCT equipment over time and to the variation in X-ray scattering characteristics due to changes in water distribution within the samples. In Fig. 4, the moisture percentage calculated using a linear interpolation between pure water and zero greyscale depth is displayed. The water transport can be seen by the increase in moisture percentage with increasing time. The precision of the water transport mechanisms

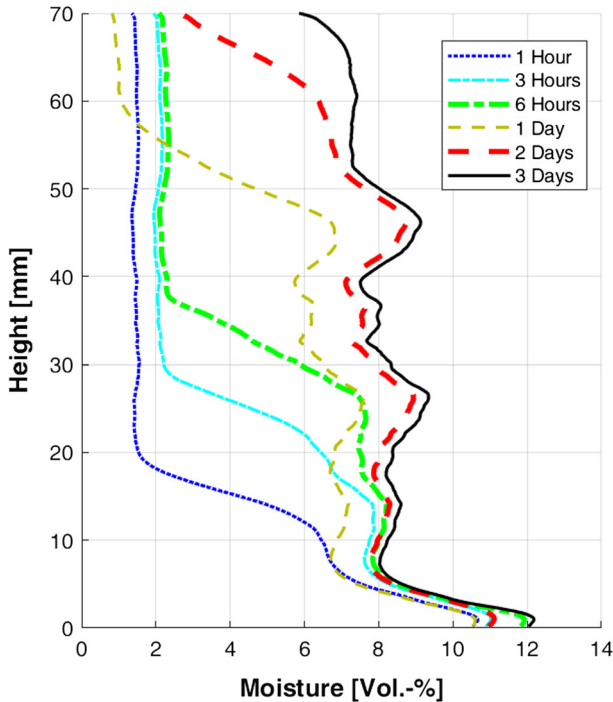


Fig. 4 Plot of measured moisture percentage change as a function of height for uncalibrated XCT images of sample 1

is, however, somewhat degraded by the presence of significant artificial offsets. The clearest example of such offsets occurs in the upper-most part of the sample (between 40 and 70 mm), which remained dry during the first 6 h of the testing process and, thus, should have exhibited a uniform (zero) moisture percentage change during this time increment. From these results, it is clear that the use of initial, uncalibrated images for making such moisture calculations was insufficient.

The moisture measurements in Fig. 4 have been expressed in terms of volume percentage (vol%). This is because, to express moisture in terms of mass percentage, the mass of the dry concrete material would have to be accounted for in the calculation (ASTM 2010). The amount of dry concrete material remains constant throughout the experiment and, thus, causes the same amount of X-ray attenuation during the acquisition of each XCT image. The presence of this material is, thus, absent from the subtraction images used to calculate moisture changes.

Nevertheless, it is true that the X-ray attenuation is directly related to the density of materials and, thus, to their mass. Liquid water held at constant temperature (as was the case during these experiments) can, however, generally be considered incompressible and, thus, to possess constant density properties (Cengel and Boles 2008). As a result, the XCT-based moisture measurements can be expressed in terms of vol%, since no frozen water was present during the experiments and the detection of any water vapour present within the samples was considered to be below the sensitivity of the measurement method. Expressing the moisture measurements in this form is the most suitable option since for vol% measurements no reference to the properties of the dry concrete materials is either needed or implied.

There are many possible causes for the offsets in Fig. 4, and it is difficult to precisely define the proportional impact of each contributing factor to the overall discrepancy between the measured greyscale depths and the true density distributions within the samples. During the scanning procedure, it was necessary for the sample to remain continuously mounted within the XCT machine so that there would be no displacements between images in subsequent scans and, as a consequence, so that direct image subtraction could occur. This meant, however, that it was not possible to acquire calibration images between each scan.

Although one possibility for overcoming this problem was to remove the sample for calibration between each scan and then align subsequent images using digital image registration prior to carrying out image subtraction, this approach was rejected for a number of reasons. First, changes in sample density and structure during the experiment could make it difficult to complete an accurate image registration following scanning. Second, the use of different calibration settings for each of the scans could lead to other offset-type effects. Third, this image analysis method was also intended for use during research on other processes where calibration between each scan is either impractical or impossible. Examples of such research include highly dynamic processes, such as thermal testing of concrete (Stelzner et al. 2017).

“Dark-field” and “bright-field” images, which correspond to blank images (i.e. containing no sample) acquired with no illumination and full illumination, respectively, are usually acquired prior to each XCT scan in order to compensate for changes in the properties of the X-ray source and the variation in the sensitivity levels of each individual detector pixel. The intensity and distribution of the X-ray beam can vary considerably because of heating and deterioration of the target material within the X-ray tube where the X-rays are generated. After long periods of scanning, residual “burn-in” image artefacts can also be present within subsequent detector images.

A second possible contributor to these image distortions is variation in X-ray scattering due to changing moisture distributions within the scan images. In addition to the direct measurement of X-ray attenuation as the beam passes through matter, the X-ray detector is also excited by X-ray beams scattered by the matter (in this case, water molecules) (Morgan and Warren 1938). These scattering patterns are complex, occur throughout the entire image, and are very difficult to isolate.

3.4.2 Calibration of the XCT Images to Mitigate the Effect of Distortions

To reduce the impact of these distortions, a calibration procedure was developed, which imposed an artificial calibration on the images to reduce the effects caused by image artefacts. The standard formula for the calibration using “dark-field” and “bright-field” images is provided in Eq. 2.

$$I_{ijk} = \left(\frac{GV_{ijk} - DF_{ijk}}{BF_{ijk} - DF_{ijk}} \right) \times SF \quad (2)$$

I_{ijk} calibrated image, GV_{ijk} uncalibrated greyscale image, DF_{ijk} dark-field calibration image, BF_{ijk} bright-field calibration image, SF scaling factor—maximum grey value (65,535 for 16 bit).

This formula is usually applied pixel-by-pixel to the 2D projection images prior to 3D image reconstruction. It is important to note that here we strive to apply this method to (already reconstructed) 3D volumes instead. In this case, the grey values of the volumes do not represent X-ray intensities directly, but rather attenuation coefficients. The difficulty lies in the determination of suitable calibration images. In the 2D case, the calibration images can be obtained by measuring the full beam without a sample (bright field) and the detector

noise when the X-ray beam is switched off (dark field). In the case of this 3D calibration, the attenuation values of dense and less dense materials at each voxel are needed to perform the calibration.

In order to make this artificial correction, material markers had to be identified within the scan images that were considered to possess near-constant X-ray attenuation throughout the experiments. It was noted that during the experiments, the coarse stone aggregate appeared to remain almost completely impervious to water (see, for instance, Fig. 2) and, therefore, the X-ray attenuation does not change. The measured attenuation, however, is influenced by the scattered radiation and the changes of the device over time. The basic idea is now to use the aggregates in the reconstructed image as a local “probe” to measure the changes caused by these influences and to correct the rest of the image using an interpolation based on these values.

Of course, for the general application of this algorithm, aggregate may not always be available to serve a material marker for the calibrations. Such is the case for mortar samples, for instance. In that scenario, an alternative object with relatively high density could be used as the material marker. Examples include, for instance, steel fibres in fibre-reinforced concrete, high-density mineral particles in sediment or heterogeneous stone, silicon sand grains in mortar or soil scanned at very high-resolution, casing materials enclosing the sample during in-situ water exposure, embedded reinforcing bars, thermocouples, or other instrumentation.

Given that the aggregate material was the brightest (i.e. the most dense) component within the reconstructed XCT images and that it possessed consistent attenuation properties, it appeared to be an ideal component to serve as the basis for an artificial “bright-field” calibration image.

The aggregates were first identified using a combination of image filtering and selection of optimal thresholds (Fig. 5b). Since the edges of the aggregate were not always accurately defined and were most likely affected by the presence of water, the aggregate in the images were then eroded so that only their cores remained (Fig. 5c). By multiplying a binary image of the aggregate cores (Fig. 5c) by the subtraction images (Fig. 5d), the change in measured density for the aggregate could then be isolated (Fig. 5e).

Assuming that the aggregate cores did not absorb significant moisture, and therefore possess a constant X-ray attenuation, the average difference between subsequent images should be zero in the aggregate cores. A three-dimensional, third-order polynomial was fitted to the difference values detected within the aggregate cores using the QR decomposition (Parlett 2000). Using this fit, a full 3D image was then constructed (Fig. 5f). This image was considered to be the “differential bright-field” image (Eq. 3). This differential bright field only represents the difference between the two (unknown) bright-field images of the two scans. It will be shown later how this can be used to perform a two-point calibration if the differential dark field is also known, which is defined by an analogous equation.

$$BF_{2ijk} = BF_{1ijk} + dBF_{ijk} \quad (3)$$

BF_{1ijk} bright-field image for initial (dry) scan, BF_{2ijk} bright-field image for subsequent (wet) scan, dBF_{ijk} differential bright-field image.

As the basis material for calculating an artificial “differential dark-field” image, air was selected. Air was ideal because it represented the least dense (and therefore darkest) component within the reconstructed XCT images and was considered to possess consistent attenuation properties throughout the scanning series. Ideally, the air voids within the sample would be used for making this calibration because they would provide a 3D material marker distributed throughout the sample. For these particular experiments, however, this was not considered to be a practical solution.

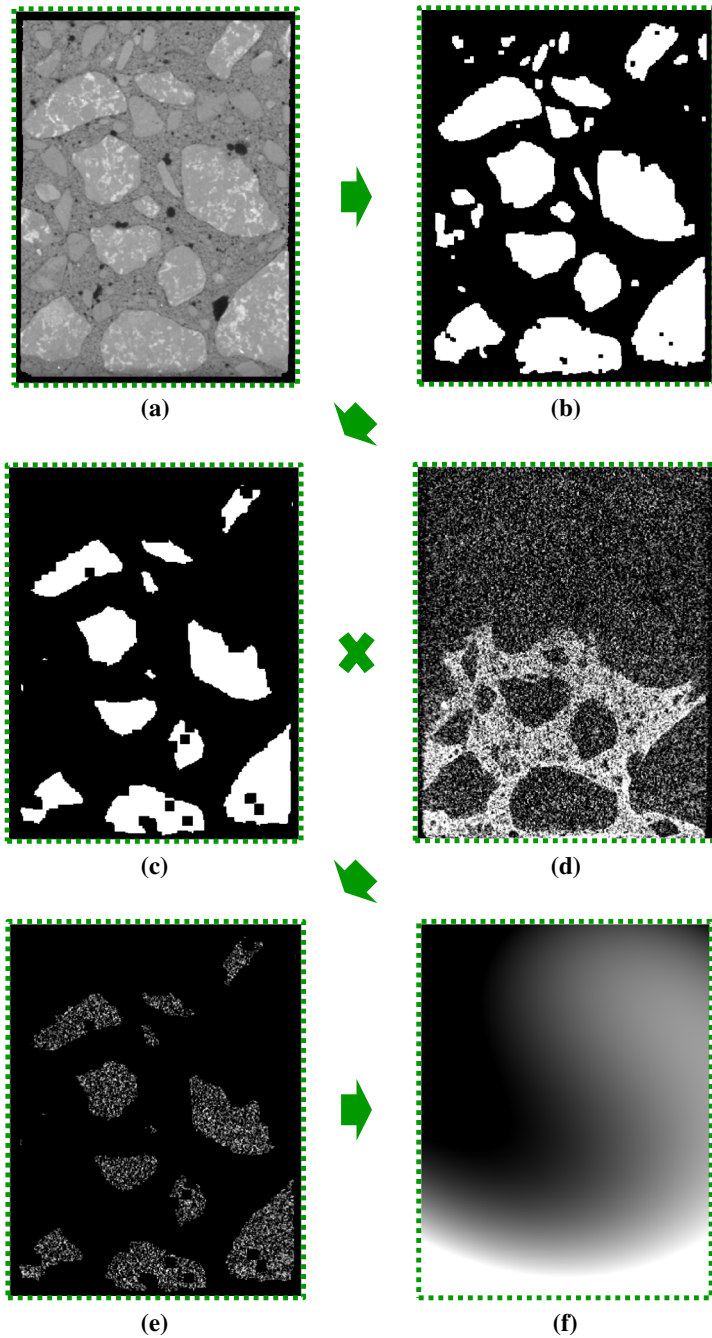


Fig. 5 Image processing for calibration of beam distortion by means of virtual “bright-field” correction: XCT image of sample 1 cross section (a), binary image of detected aggregate (b), binary image of eroded aggregate (c), subtraction image for 6-h water absorption increment (d), image of the subtraction voxel values for only the eroded aggregate (with contrast amplified for better observation) (e), and “bright-field” image (with contrast amplified for better observation) created from QR-fit of image “e” (f)

Although most of the larger air voids within the sample tended to remain unfilled by water during the experiments, the mortar matrix material around their edges did undergo moisture changes. Thus, to eliminate this effect from any subsequent calibrations, it would be necessary to erode the pore boundaries prior to using the pores for calculation of the “differential dark-field” calibration image. A similar erosion process has already been described for the aggregate “differential bright-field” calibration image markers. However, given the relatively low porosity of the concrete material used during these experiments, such an erosion process would leave insufficient remaining material in order to create a suitable fit of the “differential dark-field” calibration image. As an alternative procedure, the air region immediately surrounding the sample was selected for developing the “differential dark-field” calibration image. This region provided a large number of voxels distributed over the sample height for fitting the “differential dark-field” calibration image.

To isolate this region, the sample boundaries were identified using a procedure known as “shrink-wrapping” (Fig. 6b) (de Wolski 2011; Oesch 2015). These boundaries were then dilated until they included the entire region within the polymer sample holder. By then subtracting the original sample, this border region could be isolated (Fig. 6c). Using a procedure similar to that developed for producing the “differential bright-field” image, a binary mask of this border region was then multiplied by the original subtraction image (Fig. 6d). This provided a measurement of the deviation of the “dark-field” properties from zero, which should be the proper measurement value given the consistent density of air (Fig. 6e).

Given that it was not possible to evaluate radial variations in the differential air density, only a 1D QR-fit could be completed along the cylindrical axis. Given the limited variation in differential air density and the presence of obstructions along the edge of the sample, which limited the regions along the cylindrical axis which could be included in the calibration, only a first-order QR-fit was calculated. Using this fit, a full 3D image was then constructed (Fig. 6f). This image was considered to be the “differential dark-field” image.

By substituting the differential bright and dark fields into the two-point calibration formula (Eq. 3.), an expression for the calibrated image can be derived which does not depend on the unknown bright and dark fields. Through a reordering of the terms of this expression, Eq. 4. can then be derived. This is the final correction equation that was implemented into the MATLAB calibration algorithm.

$$D_{ijk} = \frac{I_{2o_{ijk}} - \left(\frac{dDF_{ijk}}{BF_{1ijk} - DF_{1ijk}} \right) \times SF}{1 + \frac{dBF_{ijk} - dDF_{ijk}}{BF_{1ijk} - DF_{1ijk}}} - I_{1ijk} \quad (4)$$

where $I_{2o_{ijk}}$ is the original image resulting from the reconstruction of a scan taken after water transport testing had begun. This image was initially calibrated using the “bright-field” and “dark-field” images from the initial (dry) scan. It, thus, represents the term defined by Eq. 5.

$$I_{2o_{ijk}} = \left(\frac{GV_{2ijk} - DF_{1ijk}}{BF_{1ijk} - DF_{1ijk}} \right) \times SF \quad (5)$$

Given that the initial 3D image of the dry sample was considered to be fully calibrated, there should have been no deviation from the average scalar values of the “bright-field” and “dark-field” images. Thus, the average brightnesses of the aggregate core regions and the air surrounding the sample can be used for terms BF_{1ijk} and DF_{1ijk} , respectively. Since the aggregate regions are used for fitting the “bright-field” image, the resulting, unscaled correction ratio will have a maximum value of one corresponding to aggregate brightness. Thus, the scaling factor, SF, is taken to be the average brightness in the aggregate core regions

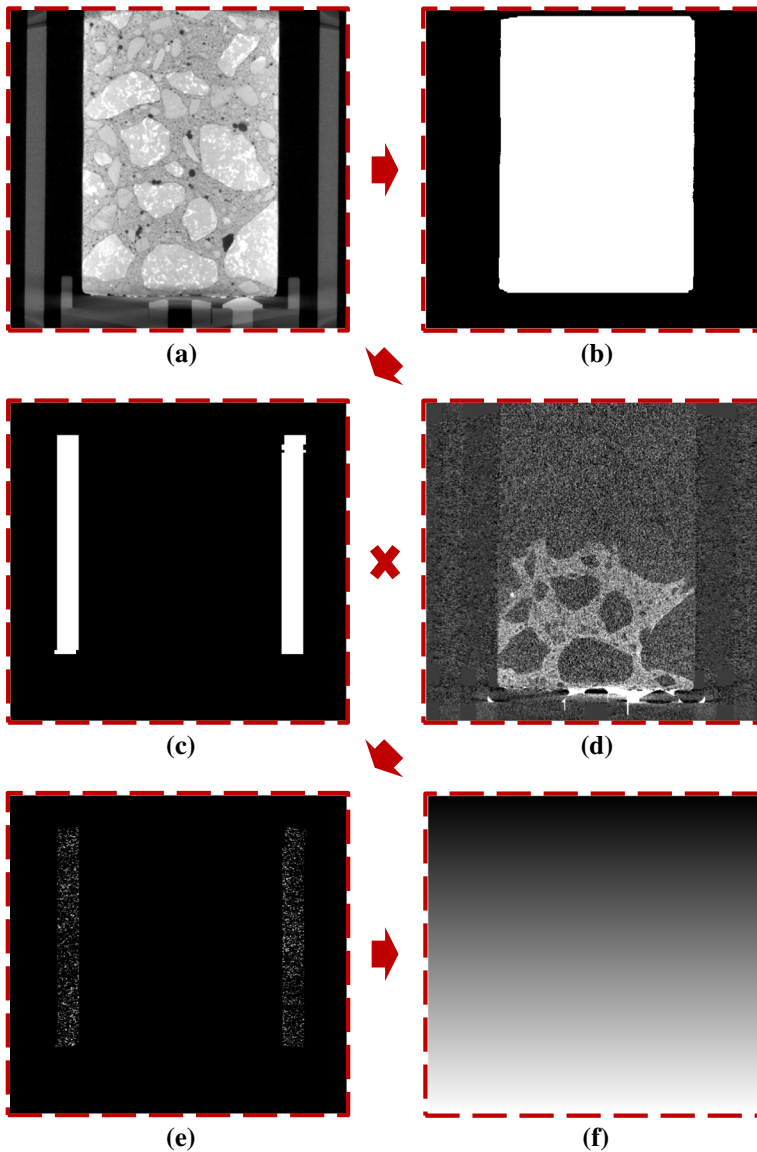


Fig. 6 Image processing for calibration of detector distortion by means of virtual “dark-field” correction: Image of sample 1 and holder (a), binary “shrink-wrap” image of sample 1 boundaries (b), surrounding air region selected for artificial “dark-field” calibration (c), subtraction image for water absorption increment (d), image of the subtraction voxel values for only the surrounding air region (with contrast amplified for better observation) (e), and “dark-field” image (with contrast amplified for better observation) created from QR-fit of image “e” (f)

in the initial dry sample image. This ensures that the resulting image is scaled to the same brightness range as the image of the dry sample. The entire image processing procedure from beginning to end is depicted as a flow diagram in Fig. 7.

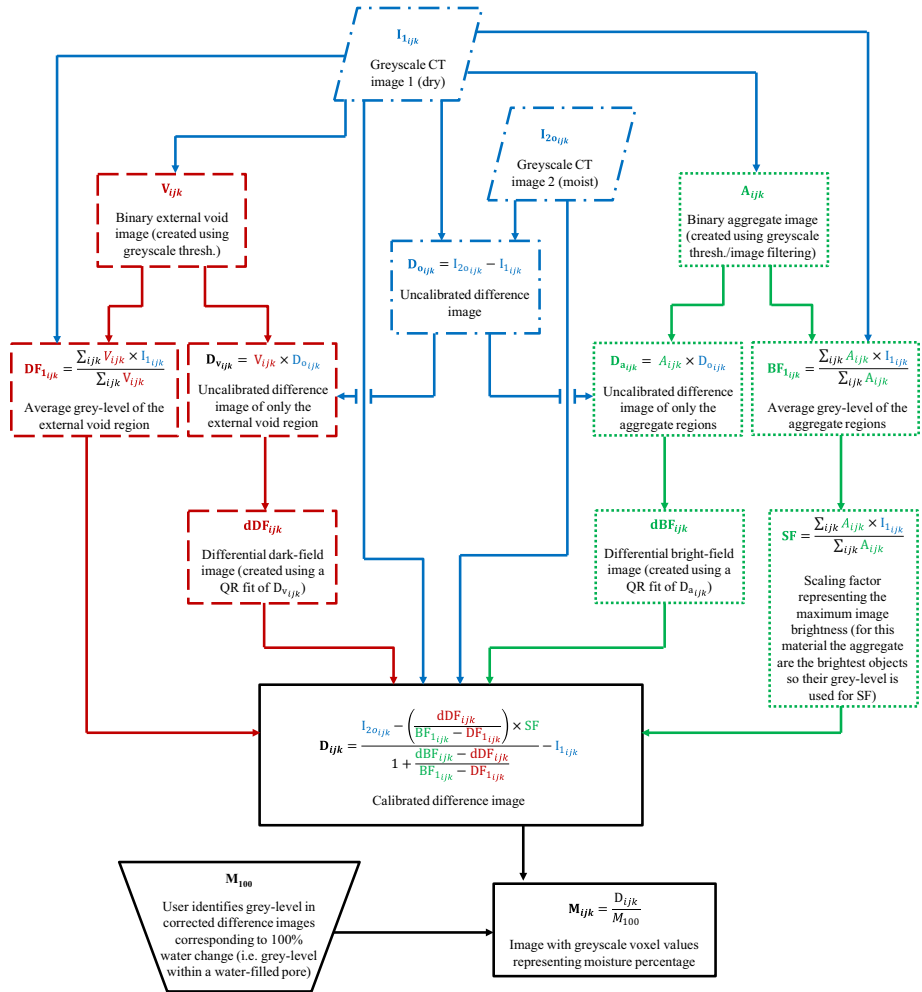


Fig. 7 Flow diagram of entire image processing procedure. Blocks with dash-dot borders represent procedures used in conventional XCT moisture measurement programs, blocks with dotted borders represent procedures used for the correction of beam distortion by means of virtual “bright-field” correction, and blocks with dashed borders represent procedures used for the correction of beam distortion by means of virtual “dark-field” correction

4 Results and Discussion

The moisture percentage diagrams obtained after applying this calibration procedure appeared to be significantly improved (Figs. 8, 9). Using this corrected data, it is also possible to visualize the 3D moisture distribution within samples at a specific time-point during in-situ testing (Fig. 10). Such direct measurements of 3D moisture distribution at different times throughout the experiments are of particular use for the numerical modelling community.

Although the corrected images in Figs. 6b and 7b appear to be significantly improved, they still contain some characteristics indicating that further, minor distortions remain within the images. Examples of these characteristics include regions within the sample at higher depth,

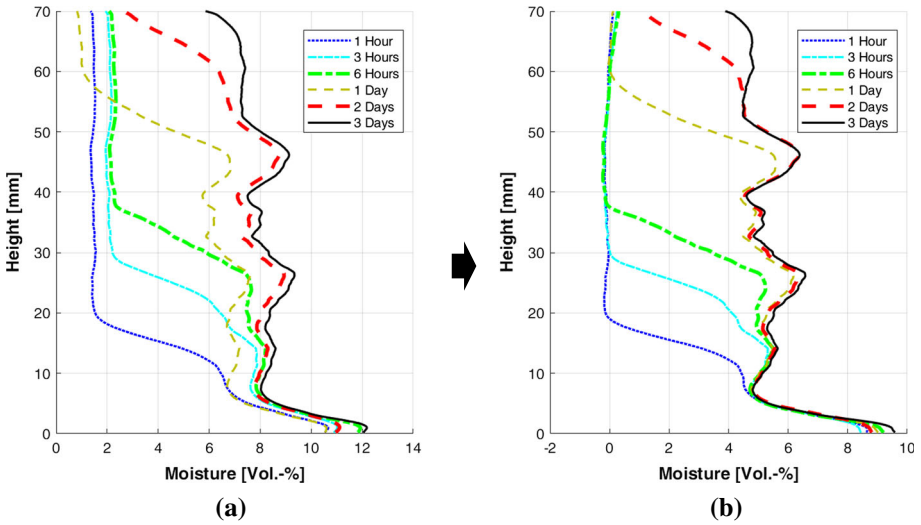


Fig. 8 Change of moisture percentage in sample 1 as a function of height calculated using the uncalibrated (a) and the calibrated (b) subtraction images

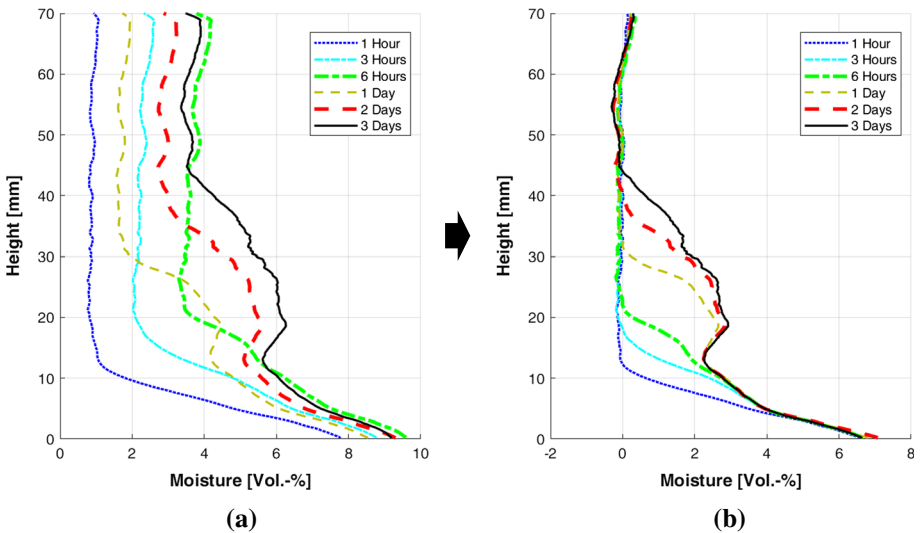


Fig. 9 Change of moisture percentage in sample 2 as a function of height calculated using the uncalibrated (a) and the calibrated (b) subtraction images

where negative changes in moisture are measured, which would indicate drying of the sample. Such negative changes, although small, are still unlikely to represent true behaviour given the short period of time, the stable atmospheric conditions, and the continuous application of water to the samples. Some deviation of the moisture characteristics among scans taken at different times within these higher depth regions of the samples can also be observed. Given the stable moisture conditions in these regions, it is unlikely that such a significant difference would arise.

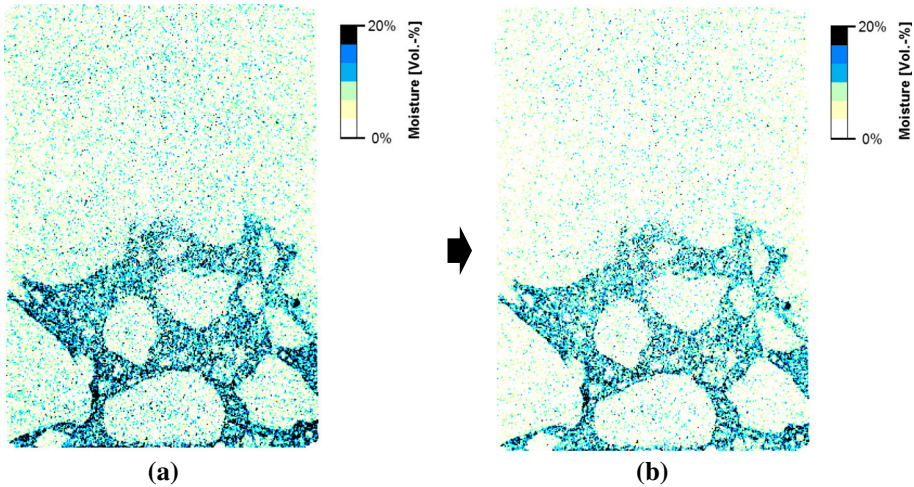


Fig. 10 Distribution of moisture change within sample 1 after 6 h of water application calculated using uncalibrated (a) and calibrated (b) subtraction images

It is thought that the magnitude of these negative values and deviations within the higher depth regions of the samples lie within the margin of error of this calibration procedure. The variable distribution of aggregate throughout the samples may lead to less accurate “bright-field” calibration within aggregate-poor sample regions. The “dark-field” calibration near the centre of the samples may also suffer from reduced accuracy given that no material from this internal region was used for the creation of the “dark-field” calibration filter.

Further, minor distortions could also be caused by sample expansion due to water absorption. This effect would typically result in artefacts along the edges of aggregates and pores within the difference images. Given the relatively low expansion that was expected for these samples relative to the image resolution and the lack of such observable artefacts in the difference images, this effect was not considered to be significant for this particular set of experiments. For samples undergoing much higher expansion or for images with significantly higher resolution, however, these effects could become significant and should be corrected for. One possible method for such a correction would be to use a digital volume correlation (DVC) program (Bay et al. 1999) to remove the effects of sample expansion from the later images of the moistened sample prior to subtraction of the initial images of the dry sample.

Most remaining distortions in the moisture images probably result from the approximate nature of the correction method used. The correction of the complex scattering and equipment variability factors on an individual basis within the unreconstructed 2D images might yield an even higher level of accuracy. Further research is also recommended which compares the results of the XCT testing program with water transport measurements from other non-destructive evaluation methods, such as NCT and 3D-NMR techniques. By conducting such a comparison, the scope and accuracy of current XCT measurement and analysis techniques could be further improved through a process of further calibration and validation.

5 Conclusions

This research demonstrated that XCT can be successfully used to measure both moisture front movement over time and changes in 3D moisture distribution within samples. The ability

to measure moisture transport in-situ in 3D represents a significant improvement of existing non-destructive moisture evaluation methods. This moisture distribution data can now be used to calibrate or validate finite element models of mass transfer in the context of ASR behaviour.

The high levels of greyscale precision required for the measurement of moisture without tracking agents result in the need for an additional image calibration procedure to correct for scatter and equipment variability artefacts arising during in-situ testing. This calibration procedure has been developed based on existing principles of XCT image correction. Resulting images of moisture distribution exhibit a high level of agreement with expected material behaviour.

The correction method described in this paper also has a wide range of applicability for analysing moisture changes in other concrete mixtures and mineral building materials. Although in this paper the image correction method has been demonstrated using low-permeability aggregate as a high-density marker material for calibrating the correction, many other component materials, intentionally placed or naturally occurring, could serve as similar markers when applying the algorithm to other materials. The important characteristics of such marker materials are that their density remains relatively unaffected by moisture changes in the rest of the sample and that they have relatively high density compared to surrounding material. Examples of promising marker materials include steel fibres in fibre-reinforced concrete, high-density mineral particles in sediment or heterogeneous stone, silicon sand grains in mortar or soil scanned at very high-resolution, casing materials enclosing the sample during in-situ water exposure, embedded reinforcing bars, thermocouples, or other instrumentation.

In addition to the undamaged beam studied in this paper, an identical beam was also cast and mechanically damaged through fatigue testing prior to XCT evaluation. These beams were prepared in order to verify the influence of mechanical pre-damage resulting from climatic and transportation impacts on the ASR deterioration within a concrete pavement. In this paper, only the results of water transport testing on two undamaged samples, denoted here as samples 1 and 2, were presented. These results were sufficient to demonstrate the accuracy and consistency of the analysis methods. Similar analyses have also been conducted on damaged samples, and a further publication comparing water transport in damaged and undamaged samples is planned.

Acknowledgements Gefördert durch die Deutsche Forschungsgemeinschaft (DFG) – Projektnummer 165295427 (Funded by the Deutsche Forschungsgemeinschaft (DFG, German Research Foundation) – project number 165295427).

Compliance with Ethical Standards

Conflict of interest The authors declare that they have no conflict of interest.

Open Access This article is distributed under the terms of the Creative Commons Attribution 4.0 International License (<http://creativecommons.org/licenses/by/4.0/>), which permits unrestricted use, distribution, and reproduction in any medium, provided you give appropriate credit to the original author(s) and the source, provide a link to the Creative Commons license, and indicate if changes were made.

References

ASTM: Standard Test Methods for Laboratory Determination of Water (Moisture) Content of Soil and Rock by Mass. ASTM International. In: ASTM D2216-10. West Conshohocken, PA (2010)

- ASTM: Standard Test Method for Field Determination of Water (Moisture) Content of Soil by the Calcium Carbide Gas Pressure Tester. ASTM International. In: ASTM D4944-18. West Conshohocken, PA (2018)
- Bay, B.K., Smith, T.S., Fyhrrie, D.P., Saad, M.: Digital volume correlation: three-dimensional strain mapping using X-ray tomography. *Exp. Mech.* **39**(3), 217–226 (1999). <https://doi.org/10.1007/Bf02323555>
- Bentz, D.P., Hansen, K.K.: Preliminary observations of water movement in cement pastes during curing using X-ray absorption. *Cem. Concr. Res.* **30**(7), 1157–1168 (2000). [https://doi.org/10.1016/S0008-8846\(00\)00273-8](https://doi.org/10.1016/S0008-8846(00)00273-8)
- Boone, M.A., De Kock, T., Bultreys, T., De Schutter, G., Vontobel, P., Van Hoorebeke, L., Cnudde, V.: 3D mapping of water in oolithic limestone at atmospheric and vacuum saturation using X-ray micro-CT differential imaging. *Mater. Charact.* **97**, 150–160 (2014). <https://doi.org/10.1016/j.matchar.2014.09.010>
- Bultreys, T., De Boever, W., Cnudde, V.: Imaging and image-based fluid transport modeling at the pore scale in geological materials: a practical introduction to the current state-of-the-art. *Earth Sci. Rev.* **155**, 93–128 (2016). <https://doi.org/10.1016/j.earscirev.2016.02.001>
- Cengel, Y.A., Boles, M.A.: *Thermodynamics: An Engineering Approach*, 6th edn. McGraw-Hill, New York, NY (2008)
- Cnudde, V., De Kock, T., Boone, M., De Boever, W., Bultreys, T., Van Stappen, J., Vandevoorde, D., Dewanckele, J., Derluyn, H., Cardenes, V., Van Hoorebeke, L.: Conservation studies of cultural heritage: X-ray imaging of dynamic processes in building materials. *Eur. J. Miner.* **27**(3), 269–278 (2015). <https://doi.org/10.1127/ejm/2015/0027-2444>
- Cnudde, V., Dierick, M., Vlassenbroeck, J., Masschaele, B., Lehmann, E., Jacobs, P., Van Hoorebeke, L.: Determination of the impregnation depth of siloxanes and ethylsilicates in porous material by neutron radiography. *J. Cult. Herit.* **8**(4), 331–338 (2007). <https://doi.org/10.1016/j.culher.2007.08.001>
- Cnudde, V., Dierick, M., Vlassenbroeck, J., Masschaele, B., Lehmann, E., Jacobs, P., Van Hoorebeke, L.: High-speed neutron radiography for monitoring the water absorption by capillarity in porous materials. *Nucl. Instrum. Methods B* **266**(1), 155–163 (2008). <https://doi.org/10.1016/j.nimb.2007.10.030>
- DAFStb: Prüfung von Beton, Empfehlung und Hinweise als Ergänzung zu DIN 1048, vol. 422. Deutscher Ausschuss für Stahlbeton (DAFStb); Beuth Verlag GmbH (1991)
- de Wolski, S.C.: shrinkWrap. In: MATLAB Program (2011)
- Derluyn, H., Griffa, M., Mannes, D., Jerjen, I., Dewanckele, J., Vontobel, P., Sheppard, A., Derome, D., Cnudde, V., Lehmann, E., Carmeliet, J.: Characterizing saline uptake and salt distributions in porous limestone with neutron radiography and X-ray micro-tomography. *J. Build. Phys.* **36**(4), 353–374 (2013). <https://doi.org/10.1177/1744259112473947>
- Dewanckele, J., De Kock, T., Fronteau, G., Derluyn, H., Vontobel, P., Dierick, M., Van Hoorebeke, L., Jacobs, P., Cnudde, V.: Neutron radiography and X-ray computed tomography for quantifying weathering and water uptake processes inside porous limestone used as building material. *Mater. Charact.* **88**, 86–99 (2014). <https://doi.org/10.1016/j.matchar.2013.12.007>
- Dierick, M., Vlassenbroeck, J., Masschaele, B., Cnudde, V., Van Hoorebeke, L., Hillenbach, A.: High-speed neutron tomography of dynamic processes. *Nucl. Instrum. Methods A* **542**(1–3), 296–301 (2005). <https://doi.org/10.1016/j.nima.2005.01.152>
- Feldkamp, L.A., Davis, L.C., Kress, J.W.: Practical cone-beam algorithm. *J. Opt. Soc. Am. A* **1**(6), 612–619 (1984). <https://doi.org/10.1364/JOSAA.1.000612>
- FGSV: Technische Lieferbedingungen für Baustoffe und Baustoffgemische für Tragschichten mit hydraulischen Bindemitteln und Fahrbahndecken aus Beton. In: *Betonbauweisen*, F.f.S.-u.V.e.V.A. (ed.) TL Beton-StB 07. Cologne, Germany (2007)
- Hillenbach, A., Engelhardt, M., Abele, H., Gähler, R.: High flux neutron imaging for high-speed radiography, dynamic tomography and strongly absorbing materials. *Nucl. Instrum. Methods A* **542**(1–3), 116–122 (2005). <https://doi.org/10.1016/j.nima.2005.01.290>
- Kaufmann, R., Yang, F., Prade, F., Griffa, M., Jerjen, I., Di Bella, C., Herzen, J., Sarapata, A., Pfeiffer, F., Lura, P., Neels, A.: Enhancing X-ray imaging of liquids in porous materials. Paper presented at the Digital Industrial Radiology and Computed Tomography (DIR 2015), Ghent, Belgium, 22–25 June 2015
- Lukovic, M., Ye, G.: Effect of moisture exchange on interface formation in the repair system studied by X-ray absorption. *Materials (Basel)* **9**(1), 2 (2015). <https://doi.org/10.3390/ma9010002>
- Masschaele, B., Dierick, M., Cnudde, V., Van Hoorebeke, L., Delputte, S., Gildemeister, A., Gaehler, R., Hillenbach, A.: High-speed thermal neutron tomography for the visualization of water repellents, consolidants and water uptake in sand and lime stones. *Radiat. Phys. Chem.* **71**(3–4), 807–808 (2004). <https://doi.org/10.1016/j.radphyschem.2004.04.102>
- Masschaele, B., Dierick, M., Van Hoorebeke, L., Jacobs, P., Vlassenbroeck, J., Cnudde, V.: Neutron CT enhancement by iterative de-blurring of neutron transmission images. *Nucl. Instrum. Methods A* **542**(1–3), 361–366 (2005). <https://doi.org/10.1016/j.nima.2005.01.162>
- Mathworks, T.: MATLAB. In: Natick, MA, USA (2018)

- Morgan, J., Warren, B.E.: X-ray analysis of the structure of water. *J. Chem. Phys.* **6**(11), 666–673 (1938). <https://doi.org/10.1063/1.1750148>
- Oesch, T.S.: Investigation of Fiber and Cracking Behavior for Conventional and Ultra-High Performance Concretes using X-ray Computed Tomography. University of Illinois, Champaign (2015)
- Parlett, B.N.: The QR algorithm. *Comput. Sci. Eng.* **2**(1), 38–42 (2000). <https://doi.org/10.1109/5992.814656>
- Pease, B.J., Scheffler, G.A., Janssen, H.: Monitoring moisture movements in building materials using X-ray attenuation: influence of beam-hardening of polychromatic X-ray photon beams. *Constr. Build. Mater.* **36**, 419–429 (2012). <https://doi.org/10.1016/j.conbuildmat.2012.04.126>
- Peng, Z., Duwig, C., Delmas, P., Gaudet, J.P., Strozzi, A.G., Charrier, P., Denis, H.: Visualization and characterization of heterogeneous water flow in double-porosity media by means of X-ray computed tomography. *Transp. Porous Med.* **110**(3), 543–564 (2015). <https://doi.org/10.1007/s11242-015-0572-z>
- RILEM: Report rep031: Advanced Testing of Cement-Based Materials during Setting and Hardening - Final Report of RILEM TC 185-ATC. In: Reinhardt, H.W., Grosse, C.U. (eds.) p. 362 (2005)
- Roels, S., Carmeliet, J.: Analysis of moisture flow in porous materials using microfocus X-ray radiography. *Int. J. Heat Mass Trans.* **49**(25–26), 4762–4772 (2006). <https://doi.org/10.1016/j.ijheatmasstransfer.2006.06.035>
- Stelzner, L., Powierza, B., Weise, F., Oesch, T., Dlugosch, R., Meng, B.: Analysis of moisture transport in unilateral-heated dense high-strength concrete. In: 5th International Workshop on Concrete Spalling Due to Fire Exposure, Borås, Sweden, 12–13 October 2017
- Van Belleghem, B., Montoya, R., Dewanckele, J., Van den Steen, N., De Graeve, I., Deconinck, J., Cnudde, V., Van Tittelboom, K., De Belie, N.: Capillary water absorption in cracked and uncracked mortar—a comparison between experimental study and finite element analysis. *Constr. Build. Mater.* **110**, 154–162 (2016)
- Van Stappen, J., De Kock, T., Boone, M.A., Olaussen, S., Cnudde, V.: Pore-scale characterisation and modelling of CO₂ flow in tight sandstones using X-ray micro-CT; Knorringfjellet Formation of the Longyearbyen CO₂ Lab. Svalbard. *Norw. J. Geol.* **94**(2–3), 201–215 (2014)
- Visvalingam, M., Tandy, J.D.: The neutron method for measuring soil moisture content—a review. *J. Soil Sci.* **23**(4), 499–511 (1972)
- Weber, B., Wyrzykowski, M., Griffa, M., Carl, S., Lehmann, E., Lura, P.: Neutron radiography of heated high-performance mortar. In: MATEC Web of Conferences, vol. 6 (2013)
- Weise, F.: Feuchtemessung im Beton-eine Gegenüberstellung gängiger Verfahren. *Messtechnik im Bauwesen* **2**, 60–68 (2008)
- Weise, F., Müller, U., Goebbels, J.: Micro computed tomography (μ -CT) for the low invasive analysis of stone. Paper Presented at the Heritage, Weathering and Conservation Conference (HWC 2006), Madrid, Spain, June 21–24
- Weise, F., Onel, Y., Goebbels, J.: Analyse des Gefüge- und Feuchtezustandes in mineralischen Baustoffen mit der Mikro-Röntgen-3D-Computertomografie. *Bauphysik* **29**(3), 194–201 (2007)
- Wildenschild, D., Hopmans, J.W., Rivers, M.L., Kent, A.J.R.: Quantitative analysis of flow processes in a sand using synchrotron-based X-ray microtomography. *Vadose Zone J.* **4**(1), 112–126 (2005). <https://doi.org/10.2113/4.1.112>
- Wildenschild, D., Hopmans, J.W., Vaz, C.M.P., Rivers, M.L., Rikard, D., Christensen, B.S.B.: Using X-ray computed tomography in hydrology: systems, resolutions, and limitations. *J. Hydrol.* **267**(3–4), 285–297 (2002)
- Yang, F., Griffa, M., Bonnin, A., Mokso, R., Di Bella, C., Munch, B., Kaufmann, R., Lura, P.: Visualization of water drying in porous materials by X-ray phase contrast imaging. *J. Microsc.* **261**(1), 88–104 (2016). <https://doi.org/10.1111/jmi.12319>
- Yang, F., Griffa, M., Hipp, A., Derluyn, H., Moonen, P., Kaufmann, R., Boone, M.N., Beckmann, F., Lura, P.: Advancing the visualization of pure water transport in porous materials by fast, talbot interferometry-based multi-contrast X-ray micro-tomography. In: Proceedings of SPIE, vol. 9967 (2016b)
- Yang, F., Prade, F., Griffa, M., Kaufmann, R., Herzen, J., Pfeiffer, F., Lura, P.: X-ray dark-field contrast imaging of water transport during hydration and drying of early-age cement-based materials. *Mater. Charact.* **142**, 560–576 (2018). <https://doi.org/10.1016/j.matchar.2018.06.021>
- Yang, L., Zhang, Y.S., Liu, Z.Y., Zhao, P., Liu, C.: In-situ tracking of water transport in cement paste using X-ray computed tomography combined with CsCl enhancing. *Mater. Lett.* **160**, 381–383 (2015). <https://doi.org/10.1016/j.matlet.2015.08.011>